

Intermediate-Stage Sintered LLZO Scaffolds for Li-Garnet Solid-State Batteries

Faruk Okur, Huanyu Zhang, Dogan Tarik Karabay, Konrad Muench, Annapaola Parrilli, Antonia Neels, Walid Dachraoui, Marta D. Rossell, Claudia Cancellieri, Lars P. H. Jeurgens, Kostiantyn V. Kravchyk,* and Maksym V. Kovalenko*

While significant progress has been achieved in the field of Li-garnet solid-state batteries, their further development, is hindered by the formation of cavities at the $\text{Li}_7\text{La}_3\text{Zr}_2\text{O}_{12}$ (LLZO)/Li interface at practically relevant current densities and areal capacities exceeding 1 mA cm^{-2} and 1 mAh cm^{-2} . As a result, the cells exhibit limited cycling stability due to the inhomogeneous distribution of the applied current density, and therefore, the formation of Li dendrites. Another aspect of high importance is associated with the development of the fabrication methodology of thin LLZO electrolytes for achieving the high energy density of Li-garnet solid-state batteries. To contribute to these two challenging problems, in this work, a facile intermediate-stage sintering method of $50\text{-}\mu\text{m}$ thin and porous LLZO membranes with a mean pore size of $2.5 \mu\text{m}$ is presented. The employment of such porous LLZO membranes not only provides an effective means of mitigating the formation of voids at the LLZO/Li interface due to the increased LLZO/Li surface area, but also maximizes achievable energy densities. It is demonstrated that fabricated porous LLZO membranes exhibit long cycling stability of over 1480 h at a current density of 0.5 mA cm^{-2} .

enable the use of Li metal anodes,^[6–10] the research on Li/LLZO interface^[11–16] and the compatibility of LLZO with current cathode chemistries^[17–21] has progressed at an impressive pace. However, despite these stunning recent developments, the electrochemical performance and energy density of batteries based on LLZO SSE are far below the required levels.^[22] This is mainly associated with the low cycling stability of Li anodes coupled with LLZO SSE at current densities exceeding 0.5 mA cm^{-2} due to the formation of the Li dendrites.^[23–25] Another missing aspect of utmost practical importance for achieving both high gravimetric and volumetric energy densities of Li-garnet solid-state batteries is the established methodology for large-scale fabrication of LLZO SSEs in the form of thin ($<50 \mu\text{m}$) LLZO membranes.

In the context of mitigating the issues associated with Li dendrites, as well as

1. Introduction

Since the discovery of $\text{Li}_7\text{La}_3\text{Zr}_2\text{O}_{12}$ (LLZO) solid-state electrolytes (SSEs) and the realization of their high potential to replace combustible organic electrolytes in Li-ion batteries^[1–5] and

aspects of the thickness of LLZO SSEs, the development of porous LLZO in the form of thin membranes has been recently targeted.^[26–29] Such porous design of LLZO appears to address problems, assumed to be the primary reasons for Li dendrites—dynamic volume changes of the Li anode and the formation of

F. Okur, H. Zhang, D. T. Karabay, K. Muench, K. V. Kravchyk, M. V. Kovalenko

Laboratory of Inorganic Chemistry
Department of Chemistry and Applied Biosciences
ETH Zürich, Zürich CH-8093, Switzerland
E-mail: kostiantyn.kravchyk@empa.ch; mvkovalenko@ethz.ch

F. Okur, H. Zhang, D. T. Karabay, K. Muench, K. V. Kravchyk, M. V. Kovalenko
Laboratory for Thin Films and Photovoltaics
Empa – Swiss Federal Laboratories for Materials Science & Technology
Dübendorf CH-8600, Switzerland

 The ORCID identification number(s) for the author(s) of this article can be found under <https://doi.org/10.1002/aenm.202203509>.

© 2023 The Authors. Advanced Energy Materials published by Wiley-VCH GmbH. This is an open access article under the terms of the Creative Commons Attribution License, which permits use, distribution and reproduction in any medium, provided the original work is properly cited.

DOI: 10.1002/aenm.202203509

A. Parrilli, A. Neels
Center for X-ray Analytics

Empa
Swiss Federal Laboratories for Materials Science & Technology
Dübendorf CH-8600, Switzerland

W. Dachraoui, M. D. Rossell
Electron Microscopy Center
Empa

Swiss Federal Laboratories for Materials Science & Technology
Dübendorf CH-8600, Switzerland

C. Cancellieri, L. P. H. Jeurgens
Laboratory for Joining Technologies & Corrosion
Empa – Swiss Federal Laboratories for Materials Science & Technology
Dübendorf CH-8600, Switzerland

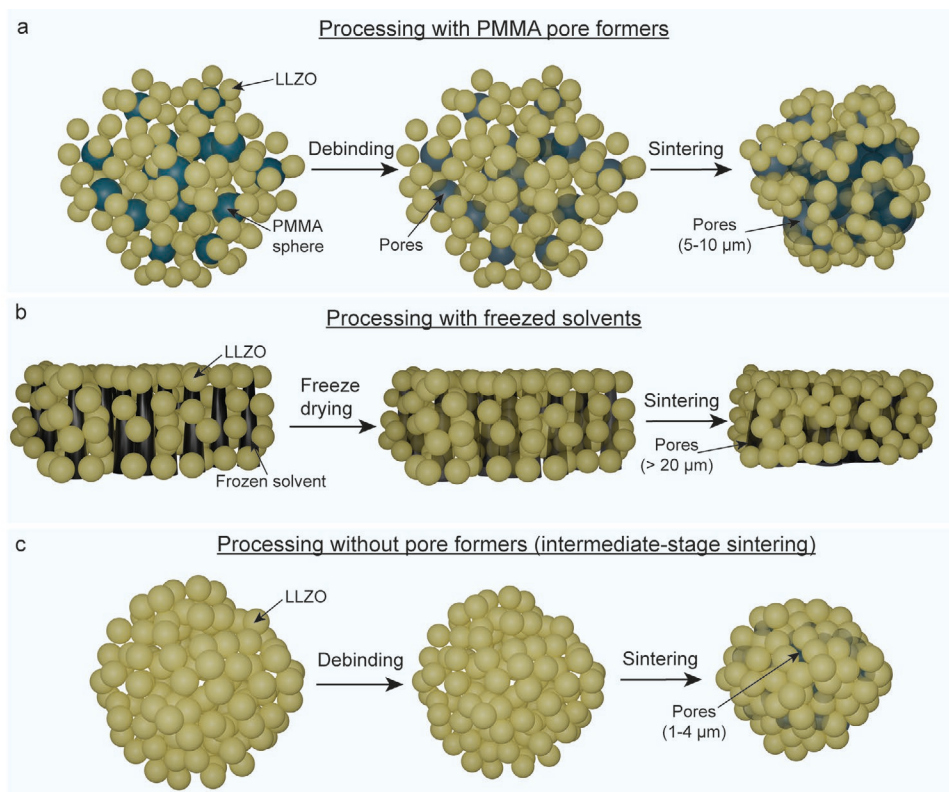


Figure 1. Schematics of different fabrication methods of porous LLZO solid-state electrolyte: a) with PMMA pore formers, b) with freezed solvents, and c) without pore formers (intermediate stage sintering).

voids.^[30–35] On the one hand, the formation of voids during stripping can be mitigated by the larger surface area of the LLZO/Li interface in the scaffold compared to dense LLZO ceramics. On the other hand, Li can be stored in the pores of the LLZO scaffold during Li deposition, thereby avoiding dynamic changes in cell volume. Thus far, several approaches have been proposed for the fabrication of porous and thin LLZO microstructures (Figure 1). In 2017, Fu et al.^[36] reported the methodology based on the addition of the poly(methyl methacrylate) (PMMA) pore fillers, enabling 5–10 μm pores during heat treatment and sintering of LLZO ceramics. In subsequent studies by Shen et al.,^[37] 50 μm porous LLZO structures were fabricated using a freeze tape casting process by employing tert-butyl alcohol crystals as pore fillers.

In this work, we present an utmost different method for the fabrication of porous LLZO membranes, which is based on intermediate-stage sintering. It is one of the simplest and most frequently used methods to fabricate porous ceramic microstructures, which is based on the termination of the sintering process before the full densification of the ceramics.^[38–40] Our primary choice was motivated by the known ability of this method to fabricate significantly smaller sizes of the pores in porous ceramics, in the range of 1 to 5 μm , potentially enabling to reach higher Li/LLZO interfacial area, as compared to the previously used template-based methods (Figure 1). We demonstrate that the presented approach enables the fabrication of self-standing, 40%-porous LLZO membranes with an open porosity of $\approx 99.7\%$ and an average pore of ≈ 2.5 μm . The developed

LLZO membranes exhibit, in symmetrical cell configuration, a high critical current density (CCD) of up to 1.15 mA cm^{-2} and low overpotentials of 5–7 mV at a current density of 0.1 mA cm^{-2} . Li plating/stripping cycling experiments of the symmetrical cells showed a high cycling stability of over 1480 h at a current density of 0.5 mA cm^{-2} with an areal capacity limitation of 0.1 mAh cm^{-2} .

2. Results and Discussion

2.1. Intermediate-Stage Sintering of LLZO Membranes

To obtain mechanically robust, well-sintered porous ceramics, an appropriate combination of sintering temperature and sintering time is required. On the one hand, it is necessary to provide conditions for a sufficient fusion of the ceramic particles to form a bulk microstructure with interconnected solid electrolyte channels. On the other hand, the sintering must be terminated early enough to prevent complete densification of the ceramic. To determine the microstructural transformations that occur during the sintering of LLZO particles, as well as the required temperature and time to obtain a porous LLZO microstructure, the LLZO sintering process was analyzed ex-situ using scanning electron microscopy (SEM) measurements at different sintering temperatures. For this experiment, we used a green-body LLZO tape, which was obtained by tape-casting of LLZO slurry on a glass substrate, followed by drying at room temperature

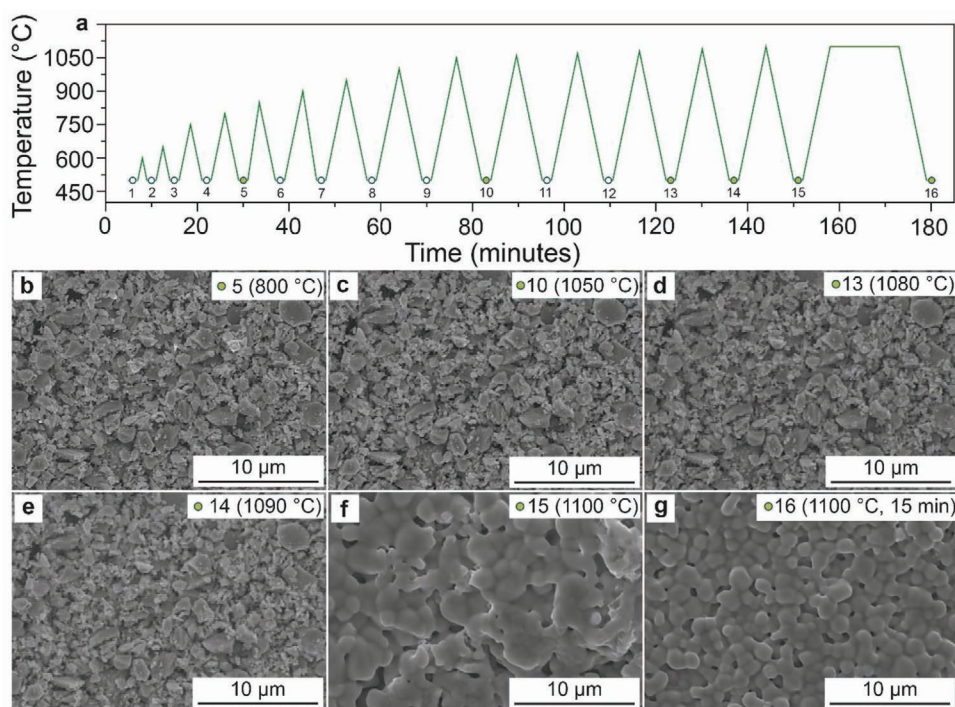


Figure 2. Ex-situ SEM measurements of LLZO membrane during sintering. a) Sintering temperature profile of LLZO membrane. The numbers on the temperature profiles represent the points at which SEM measurements of the LLZO membrane were made. b–g) Selected SEM images of LLZO membrane measured at points 5 ($T = 800\text{ }^{\circ}\text{C}$), 10 ($T = 1050\text{ }^{\circ}\text{C}$), 13 ($T = 1080\text{ }^{\circ}\text{C}$), 14 ($T = 1090\text{ }^{\circ}\text{C}$), 15 ($T = 1100\text{ }^{\circ}\text{C}$), and 16 ($T = 1100\text{ }^{\circ}\text{C}$ for 15 min). A full set of SEM images and grain size histograms of the LLZO membrane can be found in Figures S4 and S5, Supporting Information.

and annealing (debinding) at $600\text{ }^{\circ}\text{C}$ (see Experimental Section and Figure S1, Supporting Information, for details).

As shown by SEM and annular dark field scanning transmission electron microscopy (ADF-STEM) measurements, the debinded membrane consists of LLZO particles between 50 and 500 nm in size, which are weakly bound to each other (Figures S2 and S3, Supporting Information). The latter is composed of polycrystalline grains ranging from 10 to 20 nm. Interestingly, when the temperature was increased up to $1090\text{ }^{\circ}\text{C}$, almost no changes in the morphology of the LLZO particles were observed (Figure 2a–e). However, when the temperature reached $1100\text{ }^{\circ}\text{C}$ (Figure 2f), the LLZO particles began to rapidly fuse with each other. After further staying at $1100\text{ }^{\circ}\text{C}$ for 15 min (Figure 2g), the formation of a highly dense LLZO-membrane microstructure was observed.

Following obtained data on ex-situ SEM measurements and additional sintering experiments carried out in a conventional furnace (Figure 3), it was found that the optimal sintering temperature of green-body LLZO membrane is $1100\text{ }^{\circ}\text{C}$ (Figure 3a,b). Under these sintering conditions, mechanically stable microporous LLZO membranes with a porosity of $\approx 40\%$ and pore size of $\approx 2.5\text{ }\mu\text{m}$ can be obtained (Figure 3a,b,f). When lower sintering temperatures were used, highly fragile, non-sintered LLZO membranes were obtained (Figure 3c,e). Conversely, at higher sintering temperatures, the membranes were overdensified (Figure 3g,h). X-ray diffraction (XRD) and high-angle annular dark-field scanning transmission electron microscopy (HAADF-STEM) measurements of $1100\text{ }^{\circ}\text{C}$ -(15 min)-sintered membranes (Figure S6, Supporting

Information) confirmed the formation of a phase-pure cubic LLZO structure (the space group, $\text{Ia}\bar{3}\text{d}$, $a = 12.9622(2)\text{ }\text{\AA}$, $V = 2177.89\text{ }\text{\AA}^3$, ICSD 235896). The Li-ion conductivity of fabricated porous LLZO membranes was estimated at the level of $\approx 6.4 \times 10^{-4}\text{ S cm}^{-1}$, which is consistent with the measured Li-ion conductivity of fully dense LLZO membranes (see Figures S7 and S8, Supporting Information) and the reported conductivity values on LLZO pellets.^[41–43] The breaking force of the porous LLZO membranes was determined to be 70 mN (see Figure S9, Supporting Information, and Experimental Section for details).

Importantly, detailed characterization of the LLZO membranes by X-ray computed tomography revealed that the membranes have an open porosity in the range of 40–55 vol% (Figure 4) and consist of small pore sizes in the range of 1–4 μm (mean pore size of 2.5 μm). Notably, 2.5 μm is the lowest average pore size that has been reported for porous LLZO membranes so far. A detailed comparison of the reported pore sizes and porosity of porous LLZO membranes that were prepared using PMMA pore formers and freeze-dried solvents can be found in Figure S11, Supporting Information.

2.2. Surface Characterization

Next, the LLZO membranes after sintering were analyzed by Raman spectroscopy. As follows from Figure 5a, showing the existence of the D and G bands at 1344 and 1595 cm^{-1} , the surface of as-sintered membranes was contaminated with graphite.

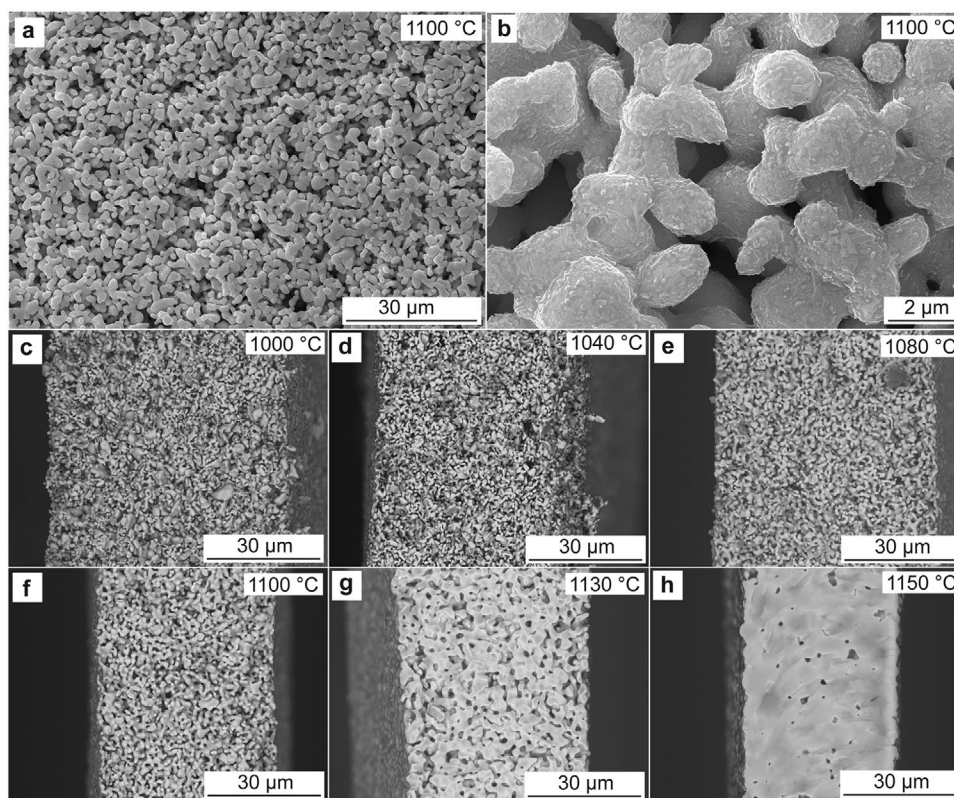


Figure 3. a,b) Top-view SEM images of LLZO membranes sintered at 1100 °C for 15 min. c–h) Cross-section SEM images of LLZO membranes sintered at different temperatures for 15 min. The sintering was performed in a conventional tube furnace under N_2 flow.

The presence of the latter is due to the graphite foil used as a substrate for sintering LLZO. In order to burn the carbon contamination from the surface, the LLZO membranes were heat treated in the air at 600 °C for 30 min. Then, the LLZO membranes were further heat-treated at 600 °C (1 h) under inert conditions (in an Ar-filled glove box). This additional heat treatment was necessary to improve the low wettability of the LLZO membranes with lithium metal, caused by $LiOH$ and Li_2CO_3 covering the LLZO surface after exposure to air. Importantly, the presence of $LiOH$ and Li_2CO_3 not only leads to an increase in the Li/LLZO interfacial resistance but also provokes the formation of Li dendrites due to the non-uniform distribution of

the applied current density.^[13,44] As confirmed by Raman spectroscopy measurements, heat treatment of LLZO membranes at 600 °C for 1 h in an Ar atmosphere significantly reduced the amount of Li_2CO_3 on the LLZO surface (Figure 5a). The Raman peak at 1090 cm^{-1} associated with the presence of Li_2CO_3 disappeared after heat treatment. It should be noted that such additional Ar-heat-treatment did not cause any structural changes in the LLZO membranes, for example, due to Li loss. Both Raman spectroscopy ($100\text{--}600\text{ cm}^{-1}$) and XRD data before and after annealing confirmed the preservation of the cubic structure of LLZO (Figure S6g, Supporting Information).

In addition to Raman spectroscopy measurements, the surfaces of LLZO membranes before and after heat treatment in an Ar atmosphere were studied by X-ray photoelectron spectroscopy (XPS). Notably, to avoid contamination of the LLZO surface due to its reaction with atmospheric water and carbon dioxide,^[45–53] the LLZO membranes were transferred to the XPS instrument under an Ar shielding gas atmosphere. Figure 5b shows the measured spectra of O 1s, C 1s, Li 1s, and Zr 3d (after charge correction, see Experimental Section for details) of LLZO membranes before and after Ar heat treatment. Analysis of the O 1s binding energies measured for non-Ar-heat-treated LLZO membranes indicates the existence of two different chemical states of oxygen. The major component of O 1s at 532.2 eV can be attributed to $Li_2CO_3/LiOH$, while a minor component at 533.8 eV is associated with $C=O$ bonding states. Binding energies of the C 1s line at 290.2 eV also confirm the presence of a Li_2CO_3 surface layer. Notably, the main C 1s peak

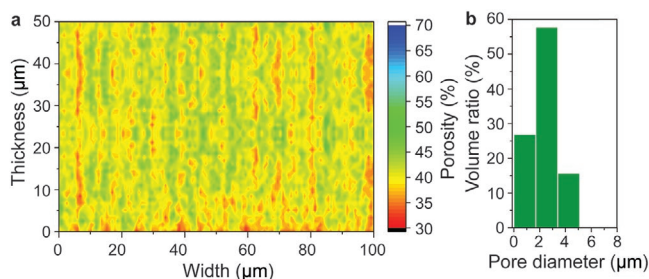


Figure 4. Average porosity distribution (a) and pore size histogram (b) inside the porous LLZO membrane, computed from X-ray computed tomography data (see Experimental Section for analysis details). The 3D image of the porous LLZO membrane (reconstructed from X-ray computed tomography data) used for porosity analysis is shown in Figure S10, Supporting Information.

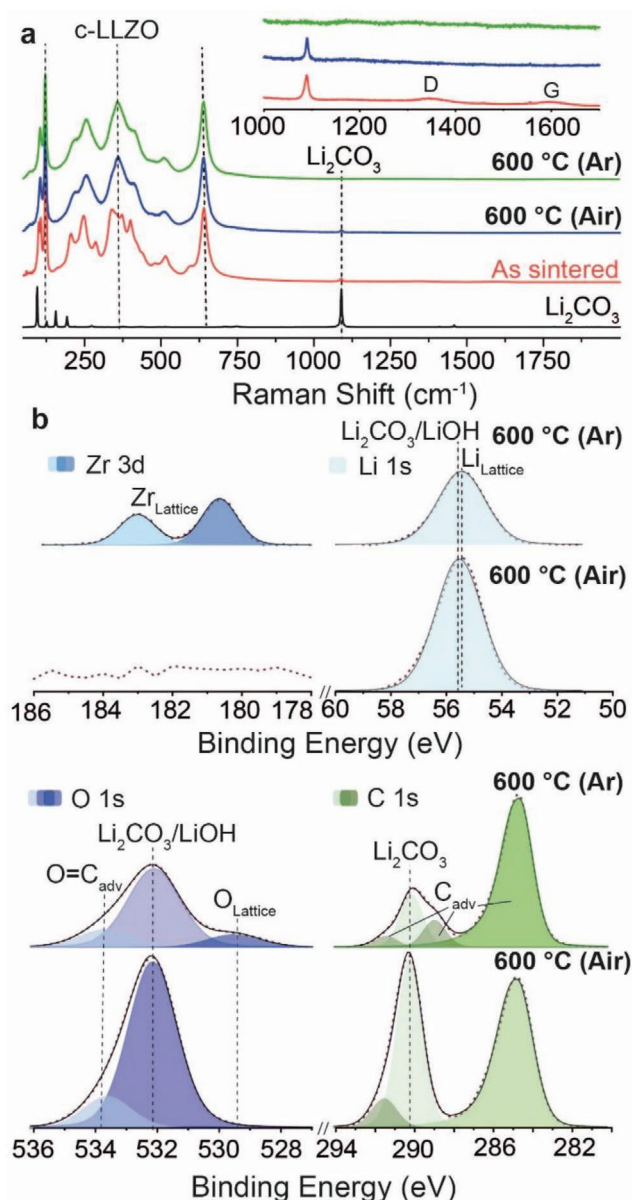


Figure 5. a) Raman spectra of LLZO membranes after sintering and subsequent heat treatment in the air (600 °C, 30 min) and then in Ar (600 °C, 1 h). Raman spectrum of Li₂CO₃ is given for comparison. b) Charge-corrected Li 1s, Zr 3d, C 1s, and O 1s XPS spectra of sintered LLZO membranes after heat treatment in the air (600 °C, 30 min) and in Ar (600 °C, 1 h).

at 284.6 eV can be attributed to the adventitious carbon (C–C bond) arising from the presence of organic species (present in the glovebox) on the surface of LLZO membranes.

Importantly, no Zr signal (178–186 eV) originating from the LLZO lattice was detected in the LLZO membrane prior to heat treatment. This indicates that the Li₂CO₃/LiOH surface layer formed on the surface of non-Ar-heat-treated LLZO membranes is much thicker than 6 nm (assuming a probing depth of ≈5.5 nm for Zr 3d photoelectrons in LLZO excited by Al-Kα X-ray radiation with $h\nu = 1486.7$ eV). Further, the XPS results clearly show that the Ar-heat-treatment of the LLZO

membranes significantly reduces the amount of Li₂CO₃/LiOH. In particular, the Zr 3d (at 183 and 180.6 eV) and O 1s (≈530.7 eV) peaks attributed to Zr and O in the LLZO lattice were clearly detected for the Ar-heat-treated LLZO membrane. This means that the effective thickness of the Li₂CO₃/LiOH layer is well below 5 nm. Furthermore, the spectral contributions of C 1s and O 1s due to the presence of Li₂CO₃ were significantly reduced. In addition, a shift of the Li 1s peak toward lower binding energies (≈55.5 to 55.3 eV) was detected, possibly due to the appearance of a spectral contribution from Li in the LLZO lattice. However, it should be noted that, given the relatively small chemical shifts of the Li 1s photoelectron lines (compared to their respective intrinsic peak widths) between different Li 1s chemical species, they cannot be unambiguously resolved.^[11]

2.3. Electrochemical Characterization

To investigate the ability of the fabricated porous LLZO microstructure to reversibly accommodate lithium metal, galvanostatic cyclic measurements of Li/LLZO/Li symmetrical cells based on self-standing porous LLZO membranes were performed. The cells were obtained by the cold isostatic pressing of two symmetrically aligned Li disks on both sides of Ar heat-treated porous LLZO membrane at a pressure of ≈71 MPa. This approach enabled to impregnate up to ≈12 μm of Li inside of the porous LLZO microstructure (Figure S12a, Supporting Information), corresponding to an areal capacity of ≈1 mAh cm⁻². Importantly, as follows from the X-ray radiography images of the fabricated Li/LLZO/Li cells (Figure S12b, Supporting Information), isostatic pressing did not cause visible mechanical damage to the membranes such as crack formation.

Electrochemical measurements were performed at a current density of 0.5 mA cm⁻² and a limiting areal capacity of 0.1 mAh cm⁻² per half cycle. As shown in Figure 6a, the Li/LLZO/Li cells exhibited high cycling stability over 1480 h, corresponding to ≈740 mAh cm⁻² of cumulative Li areal capacity. Importantly, the cells exhibited a stable overpotential of ≈70 mV throughout the cycling measurements. In contrast, control experiments performed with symmetric Li/LLZO/Li cells based on dense LLZO membranes showed low cyclic stability for only 35 h (Figure S13, Supporting Information), although the measured Li/LLZO interfacial resistance for both cells was at the same level (18 and 23 Ohm cm², see Figure S7, Supporting Information).

The achievable CCD of the systems studied, that is, the current density at which Li dendrite propagation begins was determined using galvanostatic cycling experiments at different current densities. Specifically, the current density was increased in steps from 0.05 to 1.3 mA cm⁻² in increments of 0.05 mA cm⁻², carrying 0.1 mAh cm⁻² of Li for each half cycle. As shown in Figure 6b, indicating a sharp voltage drop at the 46th half-cycle, the CCD of the Li/porous LLZO/Li symmetrical cells was ≈1.15 mA cm⁻². For comparison, analogous measurements on a symmetric cell based on dense LLZO membranes resulted in a short circuit as early as the 5th half-cycle, which corresponds to a CCD of 0.15 mA cm⁻². Importantly, additional galvanostatic measurements of Li/LLZO/Li symmetrical cells assembled

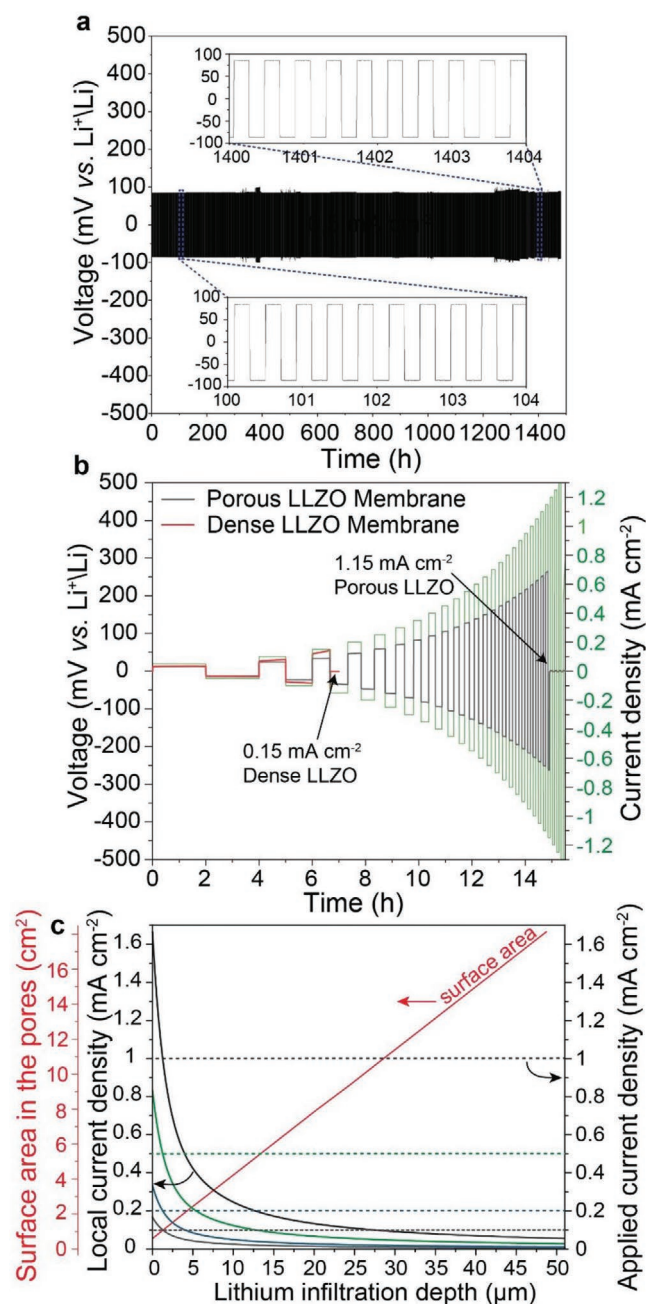


Figure 6. a) Voltage profiles of Li/porous LLZO membrane/Li symmetric cell measured at a current density of 0.5 mA cm^{-2} , the areal capacity limitation of 0.1 mAh cm^{-2} per half-cycle at room temperature. The symmetric measurements shown in (a) were intentionally stopped in order to continue the cycling at a higher capacity limitation of 0.5 mAh cm^{-2} on each half cycle while keeping the same current density of 0.5 mA cm^{-2} (see Figure S16, Supporting Information). The cycling performance of Li/porous LLZO/Li symmetrical cells measured at higher current densities of 0.5 and 1 mA cm^{-2} with the areal capacity limitation of 1 mAh cm^{-2} per half-cycle and higher temperature of 75°C is shown in the Supporting Information (see Figure S17, Supporting Information). b) Critical current density measurements of Li/porous LLZO membrane/Li and Li/dense LLZO membrane/Li symmetrical cells conducted with a capacity limitation of 0.1 mAh cm^{-2} per half-cycle. The measurements shown in (a) and (b) were performed at room temperature and without pressure. c) The surface area of the LLZO/Li interface inside the porous LLZO membrane

with porous LLZO membranes have demonstrated high cycling stability over 400 cycles at different current densities of $0.1\text{--}0.8 \text{ mA cm}^{-2}$, corresponding to the cumulative capacity of 90 mAh cm^{-2} (Figure S14, Supporting Information).

As discussed above, the high cycling stability of the microporous LLZO membrane can be explained by the partial mitigation of one of the main reasons for the appearance of Li dendrites—the formation of voids at the LLZO/Li interface, which are formed during Li stripping. The presence of such voids during subsequent Li plating leads to a significant decrease in the LLZO/Li contact area and a subsequent increase in the current density at the LLZO/Li interface, which causes the formation of Li dendrites.^[54] In this context, one advantage of porous structures is a significant increase in the contact area between LLZO and metallic lithium (see Figure S15, Supporting Information).

In our specific experiments, after infiltration of $12 \mu\text{m}$ metallic Li into the porous LLZO membrane by isostatic pressing, the actual current density at the LLZO/Li interface of the porous LLZO membrane is significantly lower than that of the dense planar LLZO membrane. For example, the current density of 0.5 mA cm^{-2} for a dense LLZO membrane corresponds to a local current density of 0.1 mA cm^{-2} applied at the LLZO/Li interface for a porous LLZO membrane (Figure 6c). This value was calculated based on the cumulative surface area of the $12 \mu\text{m}$ lithium-infiltrated region from the surface of the porous LLZO membrane (based on X-ray tomography data).

Importantly, in the case of full cells based on Li-containing cathodes, the actual LLZO/Li surface area and the corresponding current density applied to the LLZO/Li contact area will dynamically increase and decrease during charging, respectively. After discharge, they return to their original values. For example, at a current density of 1 mA cm^{-2} , at the very first moment of Li plating, the local current density for microporous LLZO membranes will be 0.2 mA cm^{-2} compared to fully dense LLZO membranes (1 mA cm^{-2}). This is explained by a fivefold larger LLZO/Li contact area compared to a fully dense LLZO (Figure 6c). When Li is further intertwined into the LLZO scaffold to 15 , 30 , and $50 \mu\text{m}$, the actual current density will continue to decrease to 170 , 100 , and $55 \mu\text{A cm}^{-2}$, respectively, for microporous LLZO membranes. A similar consideration can be applied to other current densities as shown in Figure 6c.

3. Conclusion

In summary, we have reported a simple fabrication method of microporous LLZO membranes by intermediate-stage sintering of tape-casted LLZO tapes. The underlying idea of the proposed method is based on the termination of the sintering of LLZO particles before the complete densification of the LLZO membranes. Ex-situ SEM measurements of LLZO membrane that is heat-treated at different temperatures monitored the

versus the penetration depth of electroplated Li (data are computed from X-ray computed tomography (see Experimental Section for details)). Applied current densities of 1 , 0.5 , 0.2 , and 0.1 mA cm^{-2} (dashed lines) for Li/LLZO/Li symmetrical cells based on dense LLZO membranes and the corresponding local current densities at the Li/LLZO interface in the porous LLZO membrane versus the penetration depth of electroplated Li.

morphological evolution of green-body LLZO membranes upon sintering. LLZO particles start to sinter at $\approx 1100^\circ\text{C}$ and the termination of sintering after 15 min allows to produce mechanically stable and microporous LLZO membranes. At higher temperatures or shorter sintering times, the membranes were otherwise overdensified or not well sintered, respectively. Using X-ray computed tomography, we revealed that the membranes were characterized by a mean pore size of $2.5\ \mu\text{m}$ with a narrow pore size distribution of overall porosity of $\approx 40\%$, accordingly. Importantly, no closed porosity has been detected.

After thermal purification of the surface in air and then in Ar, enabling to remove carbon and then Li_2CO_3 surface impurities, the electrochemical performance of fabricated membranes was assessed in a symmetrical Li/LLZO/Li configuration. It has been identified that the LLZO membranes are capable of fast electrochemical Li plating/stripping at a current density of up to $1.15\ \text{mA cm}^{-2}$. Cycling stability experiments demonstrated their high stability of over 1480 h at a current density of $0.5\ \text{mA cm}^{-2}$ with an areal capacity limitation of $0.1\ \text{mAh cm}^{-2}$. A side-by-side comparison of fabricated porous LLZO membranes and fully dense LLZO membranes showed that fully dense LLZO counterparts demonstrate both significantly lower CCD and poor cycling stability under identical applied electrochemical conditions. These results highlight that the use of microporous LLZO membranes is an effective approach to mitigate the issues of void formation and Li dendrites.

4. Experimental Section

Materials: Al-doped LLZO (Ampcera), Li_2CO_3 (Sigma-Aldrich), isopropanol (Emsure), ethanol (Sigma-Aldrich), 1-propanol (99.5%, AcroSeal), and polyvinyl butyral (PVPDF).

Preparation of Porous LLZO Membranes: The procedure included a few steps: i) the preparation of LLZO slurry, ii) tape-casting of LLZO slurry on the glass substrate, iii) removal of RT-dried tapes from the substrate, iv) heat treatment, and v) sintering of LLZO tapes. LLZO slurry was prepared by ball milling of LLZO and Li_2CO_3 (5 wt%), surfactant, plasticizer in solvent (5 vol% of isopropanol, 87 vol% ethanol, and 8 vol% 1-propanol) at 165 rpm for 18 h. Afterward, a binder solution (polyvinyl butyral in isopropanol) was added to the obtained suspension, followed by its further ball-milling at 200 rpm for 2 h. The LLZO slurry was tape-casted onto a glass substrate using a doctor blade with a $300\ \mu\text{m}$ opening. The prepared tape casted layer was left then for 30 min in air, peeled off from the glass substrate, and cut into small square-like samples ($\approx 1 \times 1\ \text{cm}^2$) for further processing.

Fabricated LLZO tapes were then additionally dried at 200°C for 2 h, followed by their heat treatment (debinding) at 600°C for 2 h in air. The heat treatment was performed between two porous alumina substrates to ensure the homogeneous removal of organic residuals, prevent the formation of bubbles in the sample, and maintain the flatness of the samples. The heat-treated LLZO membranes were then placed in between two graphite foils and rigid carbon plates and sintered at 1100°C (for fabrication of porous LLZO membranes) or at 1150°C (for fabrication of dense LLZO membranes) for 15 min under continuous N_2 flow. After the sintering process, the LLZO membranes were heat-treated at 600°C for 30 min under air to remove carbon residue from the LLZO surface, which originated from the used graphite foil facing LLZO. Finally, to remove interfacial layers (Li_2CO_3 , LiOH) from the surface, LLZO membranes were heat-treated in Ar filled glovebox at 600°C for 1 h.

Materials Characterization: SEM images were collected on a Hitachi TM3030Plus Tabletop microscope operated at 10 kV.

Ex situ sintering was conducted in an FEI Quanta 650 multifunctional field-emission scanning microscope operated at 10 kV, using a

Peltier/heating sample stage. Cross-sectional specimens for electron microscopy were prepared by FEI Helios Nanolab 660 FIB/SEM operated at acceleration voltages of 30 and 5 kV. The sample preparation can be summarized into five steps, which are depositing protective layers, digging pits extracting the sample, welding the sample on OMNI probe Cu grid, and thinning. HAADF-STEM and EDS elemental mapping were carried out using an FEI Titan Themis 80–300 STEM equipped with a probe Cs-corrector operated at 300 kV. The HAADF-STEM images were processed using ImageJ (Java 1.80_172 (64-bit) <https://imagej.nih.gov/ij/>) and DigitalMicrograph (Gatan) (Version 3.42.3048.0 <https://www.gatan.com>).

The mechanical strength of the porous LLZO membrane was measured using 3 point bending test on Tinius Olsen 1ST Electromechanical Testing Machine. The crosshead speed and the strain rate applied to the sample were $0.01\ \text{mm min}^{-1}$ and $2 \times 10^{-6}\ \text{s}^{-1}$, accordingly. The breaking force of the porous LLZO membrane was found to be 70 mN, which was consistent with previous studies on LLZO membranes.^[28,55] The calculated flexural strength on the breaking force was 24.1 MPa at 0.24 mm displacement. The following formulas were used to calculate flexural strength and strain rate

$$\sigma_f = \frac{3FL}{2bd^2} \quad (1)$$

and

$$\varepsilon = \frac{6ds}{L^2} \quad (2)$$

where σ_f is the flexural strength, F is the breaking force, b is the width of the LLZO membrane (8 mm), d is the thickness of the LLZO membrane ($52\ \mu\text{m}$), ε is the strain rate, s is the crosshead speed, and L is the support span (5 mm).

X-ray computed tomography measurements were performed using the EasyTom XL Ultra 230-160 micro/nano-CT scanner (RX Solutions, Chavanoz France). The scanner operated at a voltage of 90 kV and a current of 160 μA . The samples were scanned from 0° to 360° with a rotation step of 0.2° and a frame average of 10. The nominal resolution was set to 850 nm voxel size. Image reconstruction was performed using X-Act computed tomography software (RX Solutions, Chavanoz, France). Quantitative 3D and 2D analyses of the reconstructed images in 16-bit format TIFF were performed using GeoDict software.

Raman spectroscopy measurements were performed in the Ar atmosphere using a confocal Raman microscope (Horiba, LabRAM HR Evolution) equipped with an Nd:Yag 532 nm laser (Cobolt SambaTM).

XPS analysis was performed with a PHI Quantes spectrometer (ULVAC-PHI) using monochromatic Al-K α radiation (1486.6 eV; power 100 W; beam diameter of $\approx 100\ \mu\text{m}$). The XPS spectrometer was directly connected to an Ar glovebox to prevent exposure of the prepared and heat-treated membranes to air. XPS survey spectra were recorded with a pass energy of 280 eV and a step size of 0.5 eV. Detailed 1s, Zr 3d, C 1s, and O 1s regions were recorded with a step size of 0.10 eV and a pass energy of 69 eV. The energy scale of the hemispherical analyzer was calibrated according to ISO 15 472 by referencing the Au 4f $_{7/2}$ and Cu 2p $_{3/2}$ main peaks (as measured in situ for corresponding sputter-cleaned, high-purity metal references) to the recommended BE positions of 83.96 and 932.62 eV, respectively. Charge neutralization during each measurement cycle was performed with a dual-beam charge neutralization system employing low-energy electron and argon ion beams (1 V bias, 20 μA current). Measured photoelectron spectra were charge corrected using reference value for adventitious C 1s peak at 284.8 eV. The probing depths for the La 3d, O 1s, Zr 3d, C 1s, and Li 1s photoelectron lines, as recorded from LLZO using Al-K α X-ray radiation ($h\nu = 1486.7\ \text{eV}$), equal 3.6, 4.8, 5.5, 5.5, and 6.6 nm, respectively.

The level of the Li-ion conductivity of porous and dense (sintered at $T = 1150^\circ\text{C}$ for 15 min) LLZO membranes was assessed by room temperature electrochemical impedance spectroscopy (EIS) measurements in Li/LLZO/Li symmetrical cell configuration (0.62 and $0.3\ \text{mS cm}^{-1}$ for dense and porous membranes, respectively; see Figure S7, Supporting Information). Au/LLZO/Au configuration was not used because of the difficulty to make proper Au contacts for porous LLZO

membranes. The measurements were performed in a frequency range of 0.1–1 MHz with an amplitude of 10 mV (VMP3, Biologic). The ionic conductivities were calculated from the total resistance values of dense ($R_{\text{total, dense}} = 113 \text{ Ohm}$) and porous ($R_{\text{total, porous}} = 220 \text{ Ohm}$) LLZO membranes, taking into account their thickness ($h_{\text{dense}} = 50 \text{ }\mu\text{m}$; $h_{\text{porous}} = 46 \text{ }\mu\text{m}$) and the surface area of the Li electrodes ($S_{\text{dense}} = 0.071 \text{ cm}^2$, $S_{\text{porous}} = 0.071 \text{ cm}^2$). Notably, the actual ionic conductivity of porous LLZO membrane was calculated taking into consideration its porosity (low conductivity phase) as follows from the Bruggeman symmetric medium theory^[56,57]

$$\sigma_m = \sigma_h \left(1 - \frac{3}{2}f\right) \quad (3)$$

σ_m is the measured conductivity considering the geometrical dimensions of the membrane (thickness and electrode area), σ_h is the porosity corrected conductivity, and f is the volume fraction of the porosity.

To evaluate the level of activation energy of the LLZO membranes the temperature-dependent EIS measurements were performed in a frequency range of 0.1 Hz – 3 MHz with an amplitude of 10 mV (Novoelectronics) using Au/dense LLZO membrane/Au cell configuration (Figure S8, Supporting Information). Au electrodes were thermally evaporated on dense LLZO membranes using Covap thermal evaporator (Angstrom). The activation energy of the LLZO membranes was estimated at the level of 0.3 eV.

Assembly of Symmetric Cells: The fabrication of the symmetric Li/LLZO/Li cell was performed in two steps. First, to improve contact between the LLZO surface and the isostatically pressed lithium metal, 200 nm Li was thermally evaporated on both sides of the porous LLZO membrane. Then, two Li discs were symmetrically placed on the 200 nm-Li/LLZO/200-nm Li membrane and then isostatically pressed at 71 MPa for a few minutes. Isostatic pressing resulted in the impregnation of up to $\approx 12 \text{ }\mu\text{m}$ ($\approx 1 \text{ mAh cm}^{-2}$) of metallic Li inside the porous LLZO membrane. Thermal evaporation and cold isostatic pressing were conducted using the Covap thermal evaporator (Angstrom) and the PW 100 EH cold isostatic press (P/P/Weber), respectively.

Electrochemical Measurements: All electrochemical measurements were performed at room temperature or 75 °C and without external pressure in an Ar-filled glove box using a multichannel workstation (MPG -2, Bio-Logic SAS).

Supporting Information

Supporting Information is available from the Wiley Online Library or from the author.

Acknowledgements

M.V.K and K.V.K. very gratefully acknowledge Belenos Clean Power Holding Ltd. for generous funding. The authors are grateful to the research facilities of ETH Zurich (Scientific Center for Optical and Electron Microscopy and Small Molecule Crystallography Center, Department of Chemistry and Applied Biosciences) and Empa (Laboratory for Mechanics of Materials & Nanostructures). The authors acknowledge the Swiss National Science Foundation (SNSF) Research equipment (R'Equip) grant no. 182987 for supporting the XPS instrumentation used in this study. The authors thank Dorina M. Opris and Yauhen Sheima for their help with low-temperature EIS measurements.

Open access funding provided by Eidgenössische Technische Hochschule Zurich.

Conflict of Interest

The authors declare no conflict of interest.

Data Availability Statement

The data that support the findings of this study are available from the corresponding author upon reasonable request.

Keywords

$\text{Li}_7\text{La}_3\text{Zr}_2\text{O}_{12}$, Li anodes, scaffolds, solid-state batteries, solid-state electrolytes

Received: October 17, 2022

Revised: January 31, 2023

Published online: March 3, 2023

- [1] R. Murugan, V. Thangadurai, W. Weppner, *Angew. Chem., Int. Ed.* **2007**, 46, 7778.
- [2] T. Thompson, S. Yu, L. Williams, R. D. Schmidt, R. Garcia-Mendez, J. Wolfenstine, J. L. Allen, E. Kioupakis, D. J. Siegel, J. Sakamoto, *ACS Energy Lett.* **2017**, 2, 462.
- [3] A. J. Samson, K. Hofstetter, S. Bag, V. Thangadurai, *Energy Environ. Sci.* **2019**, 12, 2957.
- [4] J. Neises, W. S. Scheld, A.-R. Seok, S. Lobe, M. Finsterbusch, S. Uhlenbruck, R. Schmechel, N. Benson, *J. Mater. Chem. A* **2022**, 10, 12177.
- [5] X. Tao, L. Yang, J. Liu, Z. Zang, P. Zeng, C. Zou, L. Yi, X. Chen, X. Liu, X. Wang, *J. Alloys Compd.* **2023**, 937, 168380.
- [6] Y. S. Zhu, J. G. Connell, S. Tepavcevic, P. Zapol, R. Garcia-Mendez, N. J. Taylor, J. Sakamoto, B. J. Ingram, L. A. Curtiss, J. W. Freeland, D. D. Fong, N. M. Markovic, *Adv. Energy Mater.* **2019**, 9, 1803440.
- [7] T. Krauskopf, R. Dippel, H. Hartmann, K. Peppeler, B. Mogwitz, F. H. Richter, W. G. Zeier, J. Janek, *Joule* **2019**, 3, 2030.
- [8] J. G. Connell, T. Fuchs, H. Hartmann, T. Krauskopf, Y. Zhu, J. Sann, R. Garcia-Mendez, J. Sakamoto, S. Tepavcevic, J. r. Janek, *Chem. Mater.* **2020**, 32, 10207.
- [9] K. V. Kravchik, D. T. Karabay, M. V. Kovalenko, *Sci. Rep.* **2022**, 12, 1177.
- [10] J. Su, X. Huang, Z. Song, T. Xiu, M. E. Badding, J. Jin, Z. Wen, *Ceram. Int.* **2019**, 45, 14991.
- [11] R. Dubey, J. Sastre, C. Cancellieri, F. Okur, A. Forster, L. Pompizii, A. Priebe, Y. E. Romanyuk, L. P. H. Jeurgens, M. V. Kovalenko, K. V. Kravchik, *Adv. Energy Mater.* **2021**, 11, 2102086.
- [12] Y. Zhu, J. G. Connell, S. Tepavcevic, P. Zapol, R. Garcia-Mendez, N. J. Taylor, J. Sakamoto, B. J. Ingram, L. A. Curtiss, J. W. Freeland, *Adv. Energy Mater.* **2019**, 9, 1803440.
- [13] H. Y. Huo, Y. Chen, N. Zhao, X. T. Lin, J. Luo, X. F. Yang, Y. L. Liu, X. X. Guo, X. L. Sun, *Nano Energy* **2019**, 61, 119.
- [14] A. Sharafi, E. Kazyak, A. L. Davis, S. H. Yu, T. Thompson, D. J. Siegel, N. P. Dasgupta, J. Sakamoto, *Chem. Mater.* **2017**, 29, 7961.
- [15] M. Golozar, A. Paoletta, H. Demers, S. Savoie, G. Girard, N. Delaporte, R. Gauvin, A. Guerfi, H. Lorrman, K. Zaghib, *Sci. Rep.* **2020**, 10.
- [16] M. Cai, J. Jin, T. Xiu, Z. Song, M. E. Badding, Z. Wen, *Energy Storage Mater.* **2022**, 47, 61.
- [17] K. J. Kim, J. L. M. Rupp, *Energy Environ. Sci.* **2020**, 13, 4930.
- [18] P. Barai, T. Rojas, B. Narayanan, A. T. Ngo, L. A. Curtiss, V. Srinivasan, *Chem. Mater.* **2021**, 33, 5527.
- [19] Y. Kim, D. Kim, R. Bliem, G. Vardar, I. Waluyo, A. Hunt, J. T. Wright, J. P. Katsoudas, B. Yildiz, *Chem. Mater.* **2020**, 32, 9531.
- [20] Y. W. Dong, P. Z. Su, G. J. He, H. L. Zhao, Y. Bai, *Nanoscale* **2021**, 13, 7822.
- [21] C. Roitzheim, Y. J. Sohn, L. Y. Kuo, G. Hauschen, M. Mann, D. Sebold, M. Finsterbusch, P. Kaghazchi, O. Guillon, D. Fattakhova-Rohlfing, *ACS Appl. Energy Mater.* **2022**, 5, 6913.

- [22] K. V. Kravchyk, F. Okur, M. V. Kovalenko, *ACS Energy Lett.* **2021**, *6*, 2202.
- [23] F. Shen, M. B. Dixit, X. Xiao, K. B. Hatzell, *ACS Energy Lett.* **2018**, *3*, 1056.
- [24] D. Wang, K. Peng, Y. Fu, C. Zhu, Y. Yang, *J. Power Sources* **2021**, *487*, 229421.
- [25] F. D. Han, A. S. Westover, J. Yue, X. L. Fan, F. Wang, M. F. Chi, D. N. Leonard, N. Dudney, H. Wang, C. S. Wang, *Nat. Energy* **2019**, *4*, 187.
- [26] C. P. Yang, L. Zhang, B. Y. Liu, S. M. Xu, T. Hamann, D. McOwen, J. Q. Dai, W. Luo, Y. H. Gong, E. D. Wachsman, L. B. Hu, *Proc. Natl. Acad. Sci. U. S. A.* **2018**, *115*, 3770.
- [27] B. Y. Liu, L. Zhang, S. M. Xu, D. W. McOwen, Y. H. Gong, C. P. Yang, G. R. Pastel, H. Xie, K. Fu, J. Q. Dai, C. J. Chen, E. D. Wachsman, L. B. Hu, *Energy Storage Mater.* **2018**, *14*, 376.
- [28] G. T. Hitz, D. W. McOwen, L. Zhang, Z. H. Ma, Z. Z. Fu, Y. Wen, Y. H. Gong, J. Q. Dai, T. R. Hamann, L. B. Hu, E. D. Wachsman, *Mater. Today* **2019**, *22*, 50.
- [29] H. Zhang, F. Okur, C. Cancellieri, L. P. H. Jeurgens, A. Parrilli, D. T. Karabay, M. Nesvadba, S. Hwang, A. Neels, M. V. Kovalenko, K. V. Kravchyk, *Adv. Sci.* **2023**, 2205821.
- [30] P. Albertus, V. Anandan, C. Ban, N. Balsara, I. Belharouak, J. Buettner-Garrett, Z. Chen, C. Daniel, M. Doeff, N. J. Dudney, B. Dunn, S. J. Harris, S. Herle, E. Herbert, S. Kalnaus, J. A. Libera, D. Lu, S. Martin, B. D. McCloskey, M. T. McDowell, Y. S. Meng, J. Nanda, J. Sakamoto, E. C. Self, S. Tepavcevic, E. Wachsman, C. Wang, A. S. Westover, J. Xiao, T. Yersak, *ACS Energy Lett.* **2021**, *6*, 1399.
- [31] E. Yi, H. Shen, S. Heywood, J. Alvarado, D. Y. Parkinson, G. Chen, J. W. Sofie, M. M. Doeff, *ACS Appl. Energy Mater.* **2020**, *3*, 170.
- [32] H. Shen, E. Yi, S. Heywood, D. Y. Parkinson, G. Chen, N. Tamura, S. Sofie, K. Chen, M. M. Doeff, *ACS Appl. Mater. Interfaces* **2020**, *12*, 3494.
- [33] K. V. Kravchyk, H. Zhang, F. Okur, M. V. Kovalenko, *Acc. Mater. Res.* **2022**, *3*, 411.
- [34] F. Shen, R. A. Jonson, D. Y. Parkinson, M. C. Tucker, *J. Am. Ceram. Soc.* **2022**, *105*, 90.
- [35] K. Lee, E. Kazyak, M. J. Wang, N. P. Dasgupta, J. Sakamoto, *Joule* **2022**, *6*, 2547.
- [36] K. Fu, Y. H. Gong, G. T. Hitz, D. W. McOwen, Y. J. Li, S. M. Xu, Y. Wen, L. Zhang, C. W. Wang, G. Pastel, J. Q. Dai, B. Y. Liu, H. Xie, Y. G. Yao, E. D. Wachsman, L. B. Hu, *Energy Environ. Sci.* **2017**, *10*, 1568.
- [37] H. Shen, E. Y. Yi, M. Amores, L. Cheng, N. Tamura, D. Y. Parkinson, G. Y. Chen, K. Chen, M. Doeff, *J. Mater. Chem. A* **2019**, *7*, 20861.
- [38] F. S. Shiau, T. T. Fang, T. H. Leu, *J. Am. Ceram. Soc.* **1997**, *80*, 286.
- [39] C. Van Nguyen, S. K. Sistla, S. Van Kempen, N. A. Giang, A. Bezold, C. Broeckmann, F. Lange, *J. Ceram. Soc. Jpn.* **2016**, *124*, 301.
- [40] A. I. Waidha, V. Vanita, O. Clemens, *Ceramics* **2021**, *4*, 421.
- [41] N. J. Taylor, S. Stangeland-Molo, C. G. Haslam, A. Sharafi, T. Thompson, M. Wang, R. Garcia-Mendez, J. Sakamoto, *J. Power Sources* **2018**, *396*, 314.
- [42] S. Afyon, K. V. Kravchyk, S. Wang, J. van den Broek, C. Hänsel, M. V. Kovalenko, J. L. M. Rupp, *J. Mater. Chem.* **2019**, *7*, 21299.
- [43] V. Thangadurai, S. Narayanan, D. Pinzar, *Chem. Soc. Rev.* **2014**, *43*, 4714.
- [44] W. H. Xia, B. Y. Xu, H. A. Duan, X. Y. Tang, Y. P. Guo, H. M. Kang, H. Li, H. Z. Liu, *J. Am. Ceram. Soc.* **2017**, *100*, 2832.
- [45] L. Cheng, C. H. Wu, A. Jarry, W. Chen, Y. Ye, J. Zhu, R. Kostecki, K. Persson, J. Guo, M. Salmeron, G. Chen, M. Doeff, *ACS Appl. Mater. Interfaces* **2015**, *7*, 17649.
- [46] H. Duan, H. Zheng, Y. Zhou, B. Xu, H. Liu, *Solid State Ionics* **2018**, *318*, 45.
- [47] W. Xia, B. Xu, H. Duan, Y. Guo, H. Kang, H. Li, H. Liu, *ACS Appl. Mater. Interfaces* **2016**, *8*, 5335.
- [48] R. H. Brugge, A. K. O. Hekselman, A. Cavallaro, F. M. Pesci, R. J. Chater, J. A. Kilner, A. Aguadero, *Chem. Mater.* **2018**, *30*, 3704.
- [49] K. Hofstetter, A. J. Samson, S. Narayanan, V. Thangadurai, *J. Power Sources* **2018**, *390*, 297.
- [50] L. Cheng, E. J. Crumlin, W. Chen, R. Qiao, H. Hou, S. F. Lux, V. Zorba, R. Russo, R. Kostecki, Z. Liu, K. Persson, W. Yang, J. Cabana, T. Richardson, G. Chen, M. Doeff, *Phys. Chem. Chem. Phys.* **2014**, *16*, 18294.
- [51] L. Cheng, J. S. Park, H. Hou, V. Zorba, G. Chen, T. Richardson, J. Cabana, R. Russo, M. Doeff, *J. Mater. Chem. A* **2014**, *2*, 172.
- [52] Y. Wang, W. Lai, *J. Power Sources* **2015**, *275*, 612.
- [53] A. Sharafi, S. Yu, M. Naguib, M. Lee, C. Ma, H. M. Meyer, J. Nanda, M. Chi, D. J. Siegel, J. Sakamoto, *J. Mater. Chem. A* **2017**, *5*, 13475.
- [54] T. Krauskopf, H. Hartmann, W. G. Zeier, J. Janek, *ACS Appl. Mater. Interfaces* **2019**, *11*, 14463.
- [55] Z. Jiang, S. Wang, X. Chen, W. Yang, X. Yao, X. Hu, Q. Han, H. Wang, *Adv. Mater.* **2020**, *32*, 1906221.
- [56] D. S. McLachlan, M. Blaszkiewicz, R. E. Newnham, *J. Am. Ceram. Soc.* **1990**, *73*, 2187.
- [57] S. H. Jo, P. Muralidharan, D. K. Kim, *Solid State Ionics* **2008**, *178*, 1990.